INSTITUTE OF PHYSICS PUBLISHING JOURNAL OF PHYSICS: CONDENSED MATTER

J. Phys.: Condens. Matter **15** (2003) S3337–S3361 PII: S0953-8984(03)70847-9

Adsorbate-induced nanostructuring of vicinal surfaces: the Ag–Cu system

A R Bachmann[1,2,3], **F Ostendorf**[1,2] **and S Speller**[3,4]

[1] Fachbereich Physik, Universität Osnabrück, Barbarastraße 7, 49076 Osnabrück, Germany
[2] Physikalisches Institut, Westfälische Wilhelms-Universität Münster, Wilhelm Klemm Straße 10, 48149 Münster, Germany
[3] Institute for Molecules and Materials (NSRIM), University of Nijmegen, Toernooiveld 1, 6525 ED Nijmegen, The Netherlands

E-mail: sspeller@sci.kun.nl

Received 22 October 2003
Published 14 November 2003
Online at stacks.iop.org/JPhysCM/15/S3337

Abstract

A new possibility for producing regularly spaced nanostripes with controllable periodicity is the deposition of Ag on vicinal Cu(111) surfaces. This self-structuring originates from two different characteristic length scales of two active physical mechanisms. On the atomic scale, commensurability of Ag(111)-like structures on certain Cu planes leads to spontaneous facet formation. On the mesoscopic scale, a rippled structure is formed in which Ag and Cu nanostripes alternate. A unique property of this hill-and-valley structure is that the periodicity of the stripes can be controlled via the Ag coverage. Predictions on the basis of continuum models with long range elastic interactions can explain quantitatively the periodicities of the nanostripes.

(Some figures in this article are in colour only in the electronic version)

1. Introduction

Increasingly, the revolutionary potential of nanoscience and nanotechnology is being recognized. Although this opinion is not shared unanimously, nanoscience and nanotechnology will very likely lead to a leap in performance of devices and materials and at the same time enable completely new products. Yet, we are far away from the prospects of controlling the structural and other characteristics of materials on the scale of atoms, on the nanoscale [1]. Conventional optical lithography does not allow the fabrication of nanostructures, because light is too coarse. There are two principally different ways to produce nanostructures. Nanomanipulation by scanning probes or highly focused particle beams allows us to write nanostructures very precisely, but is inherently slow. Self-structuration is parallel, thus fast, but

[4] Author to whom any correspondence should be addressed.

so far less controllable. Future nanodevices will include elements of both types, nanostructure arrays with uniform sizes and spacings and individually written structures [2].

Compared to nanostructuration of the bulk, surfaces are directly accessible and lateral nanostructures can more easily prepared and visualized here [3]. From the results obtained during the past decade, it becomes clear that nanostructure morphologies are not very predictable and the situation is still a collection of nanostructuration recipes and mechanisms rather than comprehensive understanding at a fundamental level allowing tailoring or design. This is also reflected by the classification into self-structuration, self-assembly, self-organization, self-ordering, etc, which is not (sometimes cannot be) used in a consistent way.

Originally, self-organization referred to systems that are dynamic or not yet in equilibrium, and where the nature of interindividual interaction is mostly indirect, e.g. mediated by the surrounding gas or the bulk. With self-assembly the type of interaction is predominantly direct, for instance the phospholipid molecules in a cell membrane self-assemble mainly due to van der Waals and Coulomb interactions between direct neighbours (NNs). Also, without surrounding water the molecules self-assemble. Self-structuration, self-ordering and structure formation have been used more generally. Self-ordering is used for nanostructures that form during equilibration. It actually implies that the objects (like dots, chains or stripes) pre-exist, while self-structuration includes the formation of the objects that order. Structure formation was mostly used for growth conditions, hence kinetically determined structures, pattern formation if a diffusion–reaction mechanism is responsible, as assumed for animal coat patterns. It should be noted that although it is sometimes difficult to decide whether a structure is an equilibrium or metastable structure most patterns are referred to as self-organized.

Theoretical and experimental studies revealed that elastic interactions, stress and strain, and particularly the interplay between local and mesoscale interactions upon adsorption [4–8] play a major role in spontaneous formation of uniform nanostructures with regular sizes and spacings. Concrete, nanostructure formation could be attributed to repulsive interaction between adsorbed atoms and strain-relief patterns [9, Fe/Cu/Pt(111)], strain-mediated interactions between surface defects in strained films [10, Ag/Ru(0001)], thermodynamic size selection [11, Ag and Fe nanostructures], quantum dot growth on step bunches [12, GaAs] and competing interatomic interactions [13, Pb/Cu].

In the case of one-dimensional nanostructures one can use regular step arrays of vicinal surfaces as templates. Atomic steps often represent preferential adsorption sites, and wires and stripes can be grown by step-flow. However, if the terrace width increases to a few nanometres, single steps tend to meander and their spacing becomes irregular. Another problem is thermal disorder due to fluctuations at step edges.

Vicinal surfaces offer another way to overcome such problems at a mesoscopic scale and finite temperature, i.e. using adsorbates to induce the formation of specific facets, which are much stiffer and more time-stable than individual steps. In this case the miscut angle as well as the adatom concentration can be tuned to obtain a variety of stripe patterns that exhibit nanoelectronic effects and that are potential templates for further nanostructure growth [14–18]. The fundamental problem is controlling this complex process in order to predict and obtain useful template structures. Therefore it is important to understand the microscopic mechanisms that determine the formation of the stripe pattern.

2. Experimental set-up and procedures

We used an Omicron scanning tunnelling microscopy (STM) I set-up, equipped with Auger electron spectroscopy (AES) and low energy electron diffraction (LEED). The spot profile analysis LEED (SPALEED) was done in a different chamber at the *Freie Universität Berlin*

with a SPA-LEED set-up by Leybold-Heraeus. Cu(111) discs were cut by spark erosion from a monocrystalline Cu rod after alignment by Laue diffraction. The slices were cut into two pieces along $\langle 110 \rangle$ and wedged using a polishing machine. The resulting surfaces were mechanically and electrochemically polished to obtain a mirror-like termination [19]. The samples were mounted pairwise on the same holder. Between the back of the samples and the holder a roof was inserted in order to compensate for the wedge shape of the samples. With this mounting we achieved completely equal preparation conditions on both samples. After a short sputter-annealing treatment in ultra-high vacuum, we obtained a clean surface. All STM images were taken at 300 K. Ag deposition was done by means of an electron-beam heated source with the substrate held at 300 K. The regular stripe structure is produced after subsequent annealing to 420 K. Further annealing to 700 K does not produce any appreciable change in STM images or LEED patterns, strongly suggesting thermal equilibrium. In order to have a continuous variation of the coverage, Ag is deposited as a wedge by simply placing the Ag source in a slightly eccentric position with respect to the sample. The coverage is calculated from STM images using 3000 Å^2 frames and assuming that Ag covered areas consist of dense packed, 1 monolayer (ML) thick patches. Such assumption is consistent with the structural analysis of Ag covered areas and also with AES measurements.

3. Clean vicinal Cu(111) surfaces

3.1. Geometric properties

In face centred cubic (fcc) crystals the (111) surface is densely packed. A single (111)-layer has hexagonal symmetry with the atomic rows along the $\langle \bar{1}10 \rangle$ directions. In copper crystals the atomic separation corresponds to $a_{\parallel} = a_0/\sqrt{2} = 2.55$ Å and the distance between the atomic rows corresponds to $a_{\perp} = \sqrt{\frac{3}{8}}a_0 = 2.21$ Å. Fcc(111) planes are ABC stacked, thus adjacent (111)-layers are shifted, e.g. by $\frac{2}{3}a_{\perp}$ along the $[\bar{1}\bar{1}2]$ direction. Thus the rotation symmetry of fcc(111) surfaces is not hexagonal but trigonal and therefore also no mirror plane is present that includes $\langle 1\bar{1}0 \rangle$ directions.

As a consequence steps along the $\langle \bar{1}10 \rangle$ surface directions are physically inequivalent. The model given in figure 1 shows that the orientation of opposite $[\bar{1}10]$ steps exhibits two different minifacets, either oriented along the crystallographic [100]- or along the [111] direction. Besides the orientation of the minifacet there are further geometric differences related to the two step types. The angle the step edge minifacet includes with the (111) terrace is 35.3° for the $\{100\}$ steps and 19.5° for the $\{111\}$ steps. Further, the coordination of the ledge atoms at the steps is 10 and 11, respectively (see figure 2).

The samples measured in this work are vicinal Cu(111) surfaces with a miscut φ about the $[\bar{1}\bar{1}2]$ direction. Thus the steps are along the dense $\pm[\bar{1}10]$ directions and either exclusively $\{100\}$ or $\{111\}$ minifacets are exposed at the step edges depending on whether the miscut is clockwise or anticlockwise. We studied sample pairs with 5.0°, 7.3°, 9.0° and 11.8° miscut angles corresponding to average terrace widths of 23.8, 16.3, 13.3 and 10.2 Å. In the idealized case the surface exhibits a regular step array as shown in figure 3 for a 11.4° miscut surface with $\{100\}$ step type. The Miller index of this surface is (223). The (111) terraces are separated by monatomic $\{100\}$ steps.

In the right-hand part of figure 3 a schematic height profile along the $[\bar{1}\bar{1}2]$ direction is shown. The average step separation is given by the miscut via $d = h/\sin\varphi$, with the copper step height $h = a_0/\sqrt{3} = 2.08$ Å. The (111) terraces are of average width l and consist of four fully exposed atomic rows of width $a_{\perp}$ and one only partly (by $\frac{2}{3}\,a_{\perp}$) exposed atomic row

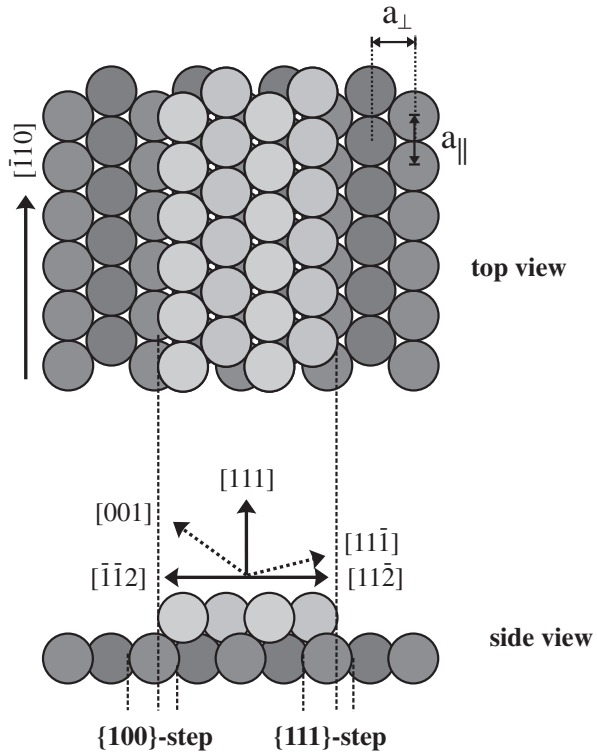

Figure 1. Sphere model of an fcc (111) surface with monatomic steps in opposite directions. At {100} steps the atomic rows at the edge of the top layer cover the lower layer (ledge atoms) by 2/3 $a_\perp$; at {111} steps they cover one-third of the ledge row.

at the ledge. For surfaces with {111} type steps the exposed ledge atomic row has a width of $\frac{1}{3}\ a_\perp$ (see also figure 3 right).

3.2. Topography and dynamical aspects

We measured the topography of clean vicinal Cu(111) surfaces with two different step types by STM and LEED. After careful preparation all surfaces exhibit a regular step array with monatomic steps, independent of the step type [20]. Figure 3 of the review by Mugarza and Ortega in this issue gives an exemplary overview of these results.

Figure 4(a) shows a typical STM topography of the Cu(223) surface. The plane of the image is chosen to coincide with the average (223) surface. The clean surface shows a regular array of monatomic, {100}-like steps along the [$\bar{1}$10] direction. The step height corresponds to the single-layer height of $h = a_0/\sqrt{3} = 2.08$ Å. The average step separation of $d = 10.2 \pm 2$ Å is measured with STM and confirmed by the spot splitting in the LEED images (see below), i.e. the surface mostly shows (223)-like terraces ($4\frac{2}{3}$ atomic rows per terrace, $d = 10.5$ Å) with a few (335)-like terraces ($3\frac{2}{3}$ atomic rows, $d = 8.4$ Å).

The period of the step superlattice can also be measured by LEED [21]. Figure 4(b) shows a conventional LEED image of the clean Cu(223) surface at 115 eV. It displays the hexagonally arranged first order ground lattice spots of the (111) terraces (separated by $2\pi/a_\perp$) as well as the split beams due to the step superlattice (separated by $2\pi/d$). Evaluation of the beam

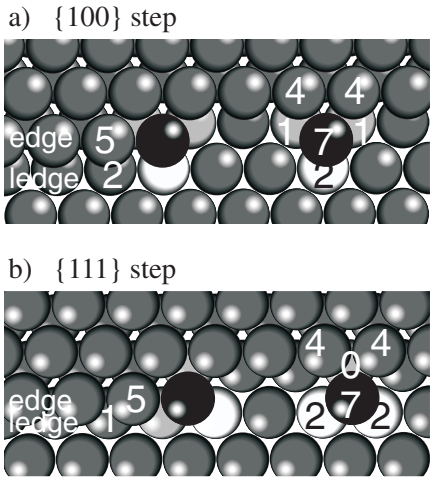

Figure 2. Sphere models of steps, kinks and adatoms at {111} and {100} steps. Step adatoms and kink atoms are shown black. Neighbour atoms with zero or one broken bond are shown light grey; neighbour atoms with two broken bonds are shown white. Atoms at the upper edges of {100} and {111} steps have five broken bonds; ledge atoms have two and one broken bonds, respectively. Step adatoms have seven broken bonds. Their direct neighbours have zero to four broken bonds and effect an attractive force to the adatom. Adatoms at a {100} ({111}) step have two (two) nearest neighbours in the upper terrace with four (four) empty bonds. Further, in the lower terrace are one nearest neighbour with two (no) empty bonds and two nearest neighbours with one (two) empty bonds each.

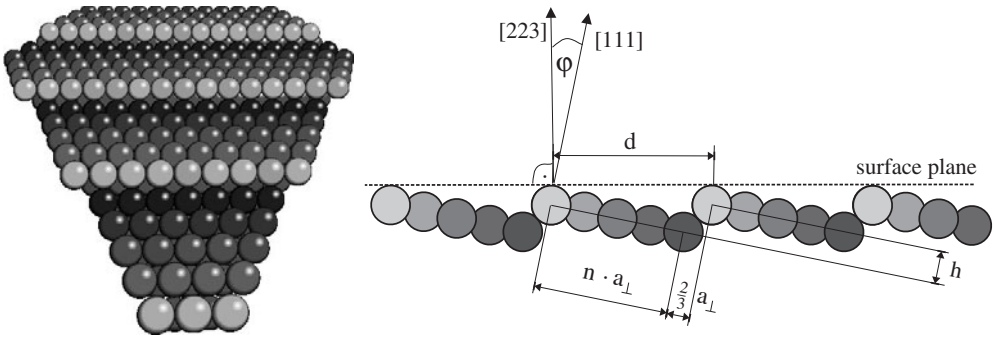

Figure 3. Sphere-model of the Cu(223) surface (exhibiting {100} type steps). Left: oblique view of the regular step array. Right: side view along the $[\bar{1}\bar{1}2]$ direction.

splitting yields an average terrace width of 10.2 Å which is in satisfactory agreement with the STM data (see below).

The intensities of the reciprocal step superlattice are modulated by the intensities stemming from the (111)-planes, leading to the characteristic beam split which is most pronounced in the so-called anti-phase condition (see figure 4(b)). For all surfaces the step superlattice periodicities measured by LEED are in agreement with the results of the STM measurements within the error bars of these methods.

3.2.1. Characterization by spot profile analysis LEED. A more refined characterization of the periodicity and coherence is possible by SPA-LEED [22–24]. In SPA-LEED the electron beam characteristics and detection are improved such that the lateral coherence length of the

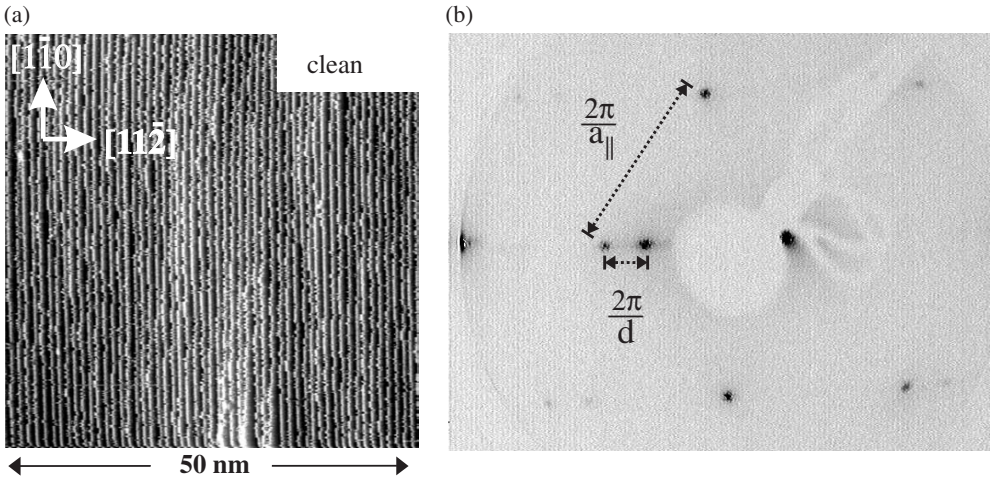

Figure 4. (a) STM topography of the clean Cu(223) surface, (500 Å)^2, from [17]. (b) LEED image (inverted grey scale) at 115 eV. The (0, 1) spot is split into two single spots, separated by the reciprocal superlattice periodicity.

beam is increased to up to thousands of ångströms. The widths of the diffraction beams are then no longer limited by the instrument but by the coherence of the surface structure. In the following we describe the results of the SPA-LEED measurements of the clean Cu(223) surface [25]. Figure 5 shows linear $k_{\parallel}$-scans along the $[-1, -1, 1]$ direction. They are shown as a grey scale plot which represents a vertical cut through the reciprocal space with the parallel and vertical k-vector as x- and y-axes. For each value of $k_{\perp}$ the electron energy had to be increased. The parallel vertical black lines represent the reciprocal scattering vectors of the (0, 1) and (0, 0) beams. In this so-called Hering plot the origin of the beam splitting becomes more obvious. Intensity is only observed in regions where the step superlattice reciprocal rods and the ground lattice modulated rods coincide. In addition the (0, 0) and (0, 1) spots show a beam-splitting caused by the regular stepped Cu surface. The separation of the (split) rods is $2\pi/d$. Thus, similar to the conventional LEED, we can determine an independent value for the step-separation by SPA-LEED of $d_{223} = 10 \pm 1$ Å. Compared to STM measurements they are found within the typical error bars. The sample miscut—here $12 \pm 0.5°$ for a Cu(223) surface—is straightforwardly derived from the inclination of the rods (at the Γ-point) to the [111] direction (dashed white line) [21]. Finally, SPA-LEED measurements can yield quantitative information of the surface condition. Therefore, one has to analyse the unique linear $k_{\parallel}$-scans along the $[-1, -1, 1]$ direction. The black arrow marks the region along $k_{\perp}$ where the anti-phase condition is fulfilled, at 100 eV (L-point). The lower part of figure 5 shows the the spot profile in detail, taken at the position of the mark. The x-axis is scaled in % Brillouin zone of the (111)-surface.

The profile of the two Cu spots in the anti-phase condition is known to be strongly influenced by the lateral order/disorder of the surface. Their analysis can give quantitative information on surface structural order within the surface area covered by the electron beam. The experimental data were fitted by a Lorentzian curve and the full width at half maximum (FWHM) thus obtained was averaged over all Cu peaks in the linear $k_{\parallel}$-scans. Because of the large transfer width in SPA-LEED the peak width is due to the finite domain size D on the surface, given approximately by $D = 2\pi/\mathrm{FWHM}$. For the clean Cu surface we obtain a domain width D of 94 ± 5 Å.

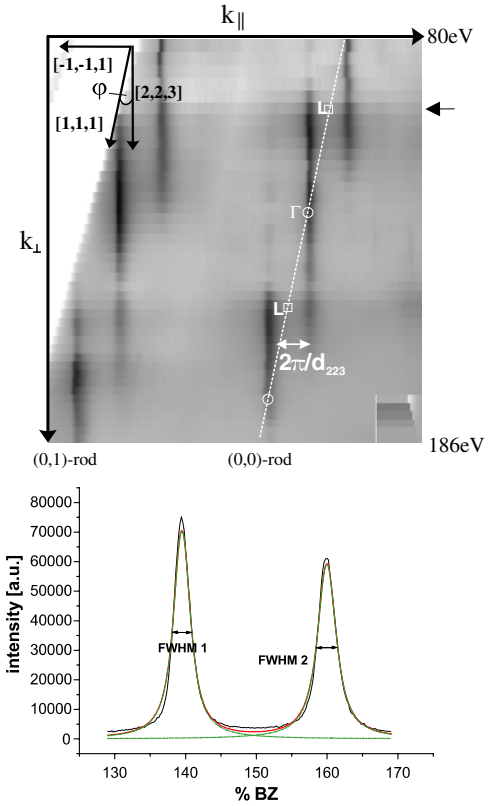

Figure 5. SPA-LEED intensity distribution. Vertical cut of reciprocal space along the (0, 1) and (0, 0) spot directions. Intensity is shown as a logarithmic grey scale plot. Vertical black lines represent the (0, 1) and (0, 0) rods. The inclination of the rods to the [1, 1, 1] direction (white dashed line) represents the miscut of the Cu(223) surface. The lower part shows the anti-phase condition of the (0, 0) spot at 100 eV in detail (marked with black arrow). The experimental data were fitted with a Lorentzian curve. From the FWHM a domain width D can be deduced.

In summary, SPA-LEED measurements of clean Cu(223) give us an average step separation of $d_{223} = 10 \pm 1$ Å, a sample miscut of $12 \pm 0.5°$ and a domain width of $D = 94 \pm 5$ Å. The domain width can be interpreted as the coherence length of the step superlattice.

3.2.2. Step arrays versus faceting. The spatial and temporal instabilities of the step arrays can originate from a weak step–step interaction or a low step free energy. In both cases it can be energetically more favourable to exhibit step bunches that alternate with large terraces than forming a regular step array. For flat Cu(111) surfaces the step energies of {100} and {111} steps are equal [26, 27].

Up to now no surface reconstruction has been found for Cu(111) vicinals with {100} step type [28, 29]. To the authors' knowledge no surface reconstruction has been observed for clean Cu(111) vicinals with {111} step type either. The only exception is an STM study of the Cu(997) surface by Giesen *et al* [26] (in combination with [30]). This surface has a miscut of $\varphi = 6.45°$ and {111} step type. A strong hill-and-valley-like structure with a complex type of triangular reconstruction has been observed, not reported for {100} step vicinals. It is difficult to decide whether the reconstruction or an ordered step array represents the equilibrium state, or whether both structures are only metastable [31].

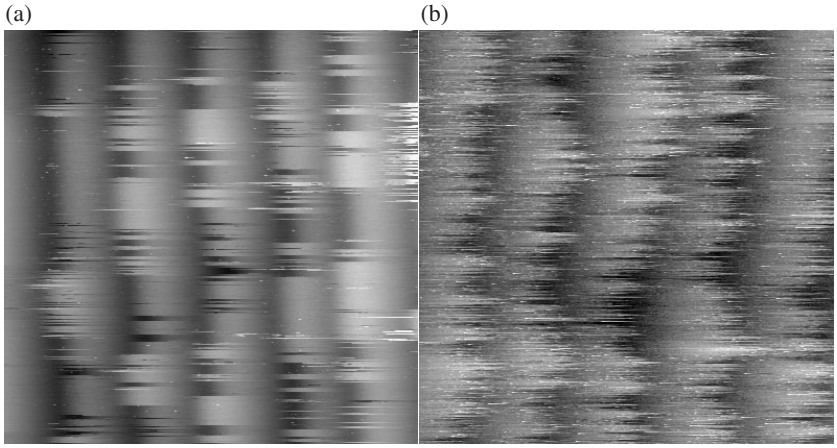

Figure 6. Comparison of STM images of vicinal surfaces with $\pm[\bar{1}10]$ steps and {100} (a) and {111} (b) minifacets. The data were taken during a step upward scan, i.e. forward (a) and backward (b), respectively. Parameters: 60 Å, 1.0 V, 0.25 nA, 385 Å s^{-1}.

This situation is in accordance with most other vicinal metal surfaces. Experimentally, it has been shown that several vicinal fcc metal surfaces exhibit a surface reconstruction. A reconstruction has been found for Ni(221) and Ni(331) surfaces [32]. Pt(997) undergoes a faceting transition at higher temperatures [33]. Temperature dependent instabilities have also been found for the surface vicinal to Pt(111) [34], Ni(111) [35], Pb(111) [36] and Au(111) [37]. Most Au(111) vicinals exhibit a facetted hill and valley structure at RT [38]. But also here a number of exceptions exist [38], i.e. Au(788), Au(322) and Au(12 12 11). These are surface orientations with a regular step array.

3.2.3. Step–step interaction. Steps on miscut low index single-crystal surfaces represent a set of one-dimensional structures. As mentioned above, in many cases, a step array of high regularity is formed due to the repulsive interaction between steps [39–42]. For soft materials, e.g. Pb, Ag, Cu etc, the step edges appear frizzled in STM images. Still, the question of whether this frizziness is induced by tip–surface interaction or merely due to step dynamics appears not to be answered completely. For Ag(110) tip–surface interaction appears to contribute even at high tunnel resistances (some GΩ) [43], whereas for Cu(111) it is concluded that the frizziness mainly carries information on the step dynamics [29].

In the following we compare the frizziness of two vicinal surfaces with equal terrace widths (i.e. $\varphi = 9°$, d 13.2 Å) but different orientations of the step's minifacets. For these systems we observe that for tunnel resistances beyond approximately 2 GΩ tip–surface interaction cannot be reduced further, and assume the frizziness in this regime to be mainly due to step dynamics. Furthermore, we show how the step mobility and the step–step interaction vary with the step type and the terrace width.

Figure 6 shows small scale STM images of the 9° samples. The parallel steps run from top to bottom. The upward direction of the steps is from left to right for the {100} steps (figure 6(a)) and from right to left for the {111} steps (figure 6(b)). On both types of sample the steps are monatomic and arrange themselves regularly. In STM images the step edges exhibit so-called frizziness. If tip–surface interaction is negligible (see below) this indicates that atoms move along step edges and that the STM under-samples the topography in time. At room temperature this is a typical feature of materials with relatively low binding energy.

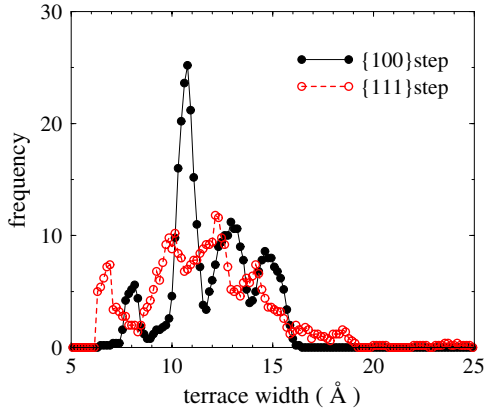

Figure 7. Comparison of TWDs from vicinal surfaces with $[\bar{1}10]$ steps and {100} and {111} step types. The maxima are separated by 2.2 Å. Maxima of the curve from the surface with {111} steps are shifted by one-third of the row separation (0.74 Å) to lower terrace widths with respect to the maxima from the surface with {100} steps. The step edges of the {100} steps are found more often in a proper fcc lattice position than the {111} step edges. The mean terrace widths are $\langle l \rangle_{\text{open}} = 12.0$ Å and $\langle l \rangle_{\text{closed}} = 11.7$ Å. The scan speed was 385 Å s^{-1}.

The main observation with the STM images is that the frizziness at the {111} steps is stronger. Note that the images are taken with equal parameters and after the *very same* preparation. Also the scan direction is equivalent (step upwards) in both cases. The difference in the extent of frizziness does not depend on whether time (scanning only on one line) or space (conventional) images are regarded.

For the quantitative analyses of the frizzes we used images of areas far away from any contamination. Such undisturbed step arrays show mean terrace widths that are very close to the nominal terrace width of the surface. In order to locate the step positions we employ a pattern matching procedure that is based on the evaluation of the slopes of the topographs. The routine purges spikes. The frequencies of the step positions are shown as a histogram (figure 7). There is a large difference in the degree of quantization of the observed terrace widths l among the two surfaces. Here, the interval size of the histogram corresponds to the spatial width of one pixel in the STM frames. The maxima in such terrace width distributions (TWDs) are separated by approximately 2.2 Å in both cases, for the {100} and the {111} step type. This is in accordance with the value of $a_\perp$, the distance between the atomic rows along $[\bar{1}\bar{1}2]$. Maxima in the distribution of the {111} step type surface are shifted by approximately $-\frac{1}{3}a_\perp = -0.74$ Å with respect to the maxima of the {100} step type surface. This reflects fcc compatibility leading to different possible terrace widths for the two step types. Proper terrace widths with {100} ({111}) steps are $d_{\{100\}\text{ step}} = (n + \frac{2}{3})a_\perp$ and $d_{\{111\}\text{ step}} = (n + \frac{1}{3})a_\perp$.

From figure 7 it is evident that step edges of {100} steps are more often in proper fcc lattice positions than the {111} step edges. In particular, the {100} step edge atoms spend the predominant part of their time (≈90%) in fcc hollow sites, indicating that their jump rate is moderate compared to the sampling rate (here 2.5 kHz). In contrast, terraces on vicinal surfaces with {111} steps are found ≈45% of their time with fcc-incompatible widths, i.e. step edges are often located outside fcc hollow sites. Usually this kind of intermediate site is not an equilibrium position but only temporarily taken during diffusion processes.

As a general trend the quantization gets more pronounced with smaller terraces (larger miscut angle); see e.g. the histogram in figure 8 of the 11° miscut surface. This can directly

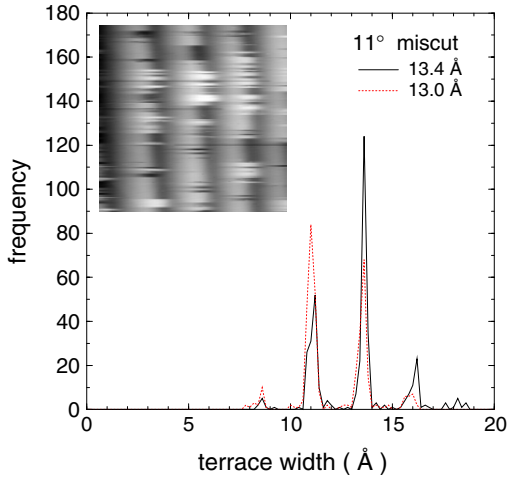

Figure 8. TWDs from the 11° miscut sample with {100} step type. The inset displays the $(50\ \text{Å})^2$ topography where this analysis has been performed. The maxima are much sharper compared to the 9° miscut sample with identical step type (figure 7(a)).

be explained by the increased repulsive step–step interaction at smaller terraces that forces the steps into a step array with stricter regularity.

In the next step of the evaluation the quantization in the TWD has been erased by choosing $a_\perp$ to be the channel width (not shown). Curves from several images have been used (dynamic scaling). The main result is that the TWDs are always wider for the {111} steps compared to the {100} step type surface. Gaussian fits to the TWD yield standard deviations of $\sigma_{\{100\}} = (0.185 \pm 0.03)\langle l\rangle$ and $\sigma_{\{111\}} = (0.26 \pm 0.02)\langle l\rangle$ with $\langle l\rangle$ denoting the mean terrace width. For both step types the ratio of standard deviation and mean terrace width $\sigma/\langle l\rangle$ is far below the maximum of 0.424, characteristic for purely entropic repulsion[5] [44], and also below 0.405, which marks a roughening transition [45]. The observation that $\sigma_{\{100\}}$ is smaller than $\sigma_{\{111\}}$ reflects that the step superlattice is much better defined for {100}step type surfaces.

3.2.4. Influence of the tip. The anisotropy in the step–step interaction as inferred above has to be corroborated further by exclusion of external influences. A potential artificial source of frizziness is the interaction between surface and tip [46, 47]. Its strength varies with material, surface orientation and tip configuration. For {100} steps on Cu(111) the influence of the tip on time correlation functions was found to be negligible when the tunnel parameters are moderate [48]. With the frizzes in conventional (space) images that we analyse in this study, the contribution from tip–surface interaction is negligible since the tunnel resistance was increased until no further reduction of the frizziness could be observed. An example is shown in figure 9 for {100} steps. Working at 100 pA tunnel current there was no further reduction of the frizziness after going beyond 2 GΩ gap resistance (figure 9). The extent of the frizzes is *then* independent on the scan direction.

3.2.5. Towards an explanation for the anisotropic step–step interaction. A possible explanation for the different extents of frizziness is a difference in diffusion mechanisms and barriers. Usually the diffusion speed depends on the corrugation of the effective diffusion

[5] For purely entropic interaction the Gaussian distribution is actually an approximation only.

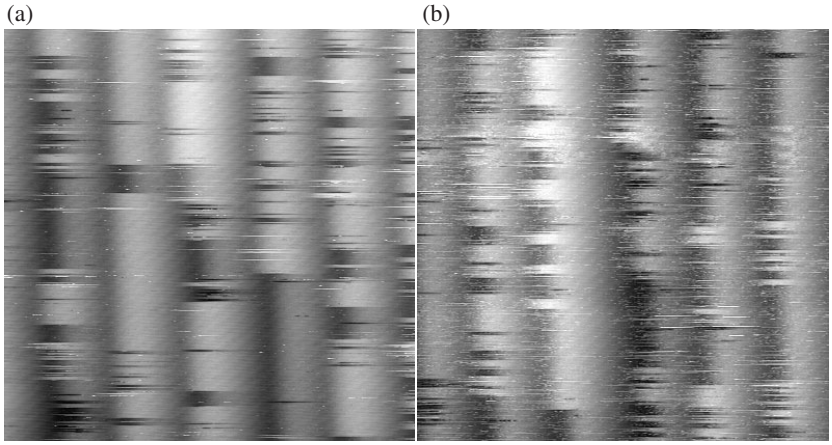

Figure 9. Images of the identical area (60 Å)^2 on the vicinal surface with $\pm[\bar{1}10]$ steps and {100} minifacets at the step edges. When lowering the tunnel resistance enhanced frizziness due to tip–surface interaction arises. The data have been taken during a step upward scan (forward). Parameters: 38.5 nm s^{-1}; 1.0 V, 0.1 nA (a); 84 mV, 0.1 nA (b).

potential, which in turn depends on the difference between the coordination of the attached adatom and the coordination of the adatom in the transition geometry, i.e. during the jump. Playing with marbles, diffusion along 100 steps feels easier because no intermediate short bridge position has to be taken. Nanoscopically, with atoms, the effective diffusion speed along the steps depends on the electronic structure of the material. For Pt(111) edge diffusion along {111} faceted steps was found to be faster, while on Rh(111) diffusion along {100} faceted steps was found to be faster in theoretical studies [49, 50]. It has to be noted that along {111} type steps the diffusion via exchange of atoms is more prominent, while along {100} faceted steps normal hopping is rather the case; this was concluded for Ag(111) [51]. Thus, to predict the effective diffusion speeds one would have to take into account all possible diffusion mechanisms and weight them according to the respective energy barriers.

It is instructive to compare the geometric situation of the adatoms at {100}and {111}type steps (see also figure 2): step adatoms have seven, their NNs zero to four broken bonds, which leads to an attractive force on the adatom. An adatom at a {100} ({111}) step has two (two) nearest neighbours in the upper terrace with four (four) empty bonds. Furthermore, in the lower terrace there is one NN with two (no) empty bonds and two NNs with one (two) empty bonds each. Thus, the total number of broken bonds is the same, although the geometrical arrangement differs. Without adatoms the higher number of broken bonds of the ledge atoms at the {100} steps will eventually lead to a stronger attaching force on adatoms and make diffusion slower. On the other hand, during diffusion along the {111} type step a long bridge position has to be taken temporarily, while along the 100 microfacet a short bridge position is taken.

Hence, one may note that diffusion in total (exchange plus edge diffusion), which is probably observed in the experiment, appears faster for adatom motion along {111} steps and is lower than along steps of {100} type. This also explains why {111} type steps are located more often outside fcc sites (figure 7). Slower diffusion should however not affect equilibrium properties, such as kink density, kink formation energy and stiffness, because diffusion is effective in both cases on the timescale of the observation.

Steps on vicinal Cu(100) [28, 41] as well as {100} steps on vicinal Cu(111) [28, 52] have been studied earlier by STM. {100} steps on vicinal Cu(111) and ⟨110⟩ steps on vicinal Cu(100) (that have minifacets of {111} type) have TWDs with almost equal Gaussian standard

deviations of 0.258 and 0.250$\langle l \rangle$ at room temperature. The value for the {100}steps on Cu(111) is high compared to this study (0.185$\langle l \rangle$), but is close to our value for the {111} steps (0.26$\langle l \rangle$). This analysis shows that it is in principle possible to obtain quantitative information on the step fluctuation statistics and eventually on the interaction potential, but the scattering among independent studies is large.

Regarding the strength of step–step-interaction among {111} and {100} steps, the contrast is clear and possible origins are discussed. In principle there are three contributions: entropic, electronic and elastic interaction. Elastic interaction occurs when the displacement fields from steps substantially superpose. The line dipoles at steps are due to Smoluchowski smoothing [53] and interact electronically. Entropic interaction is due to the condition that steps may not cross and leads to an effective repulsive potential, the weakest interaction type, always present. Entropic interaction is irrelevant with Cu(111) since all determined σ-values are rather small. On Ag(111) step dipoles did not show a significant difference [51], and we consider this also as likely for the steps on Cu(111). Thus, differences in the displacement fields of {100} and {111} steps might be a possible origin for the different interaction strengths. Calculations revealed that relaxation displacement fields differ clearly for {100} and {111} steps [54].

Summarizing this part, {100} and {111} steps on Cu(111) have been compared directly, minimizing differences in tunnel parameters, tip conditions and preparation. An anisotropy of the standard deviation of the TWDs has been found. The difference in frizziness can be explained by the contrast in the step–step repulsion which in turn is attributed to different force fields between atoms in the vicinity of steps and the surface. The contrast in the standard deviations of the TWD is most likely due to the different elastic fields at the steps.

4. Adsorption of Ag on vicinal Cu(111)

Adsorption of submonolayer amounts of Ag induces a periodic faceting of the substrate. The equilibrium structure is characterized by Ag-covered facets that alternate with clean Cu stripes. We studied the morphology of the system as a function of Ag coverage by means of STM, LEED and SPA-LEED [20]. The Ag adsorption was studied with the above mentioned {100} and {111} step type samples as well. With this set of samples several tests were done under the same preparation conditions. Qualitatively we observed the same equilibrium structure on the other vicinal Cu surfaces as well. But the detailed microscopic structure of the facets depends strongly on the surface parameters such as miscut and step type. In the following we will restrict ourselves to the quantitative analysis of the Ag adsorption on Cu(223). A stable hill and valley structure was initially observed with this substrate. Moreover—as shown above—the step dynamics are less pronounced on the {100} step type sample. Therefore, the stability of the Cu(223) surface in combination with the high step density of the substrate gives the best premises for a detailed study.

4.1. Evolution of the stripe structure with coverage

In figure 10 the evolution of the faceted structure with coverage as deduced from the analysis is depicted as a side view. As shown below, upon Ag adsorption the system undergoes faceting. Below 1 ML it is rather straightforward to distinguish three different regimes, which differ in the crystallographic orientation of the Ag-covered facet. These are

- the A regime up to ∼0.52 ML,
- the B regime between ∼0.52 and ∼0.76 ML and
- the C regime from ∼0.76 to 1 ML.

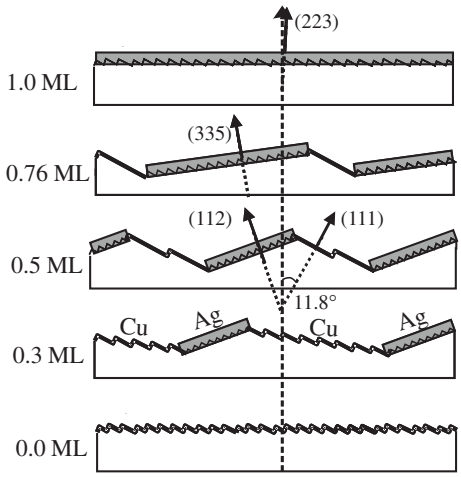

Figure 10. Schematic evolution of the periodic faceting induced by Ag on vicinal Cu(111) with 11.8° miscut, as deduced from the STM-LEED–SPA-LEED analysis.

The STM measurements in this system were made with tunnelling parameters above 10 GΩ tunnelling resistance (typically $I_t = 0.1$ nA and $U_t = 1.5$ V). The interaction of the STM tip with the Ag adlayer is not negligible. We noticed that the scanning tip can destroy the whole equilibrium structure in the scanned area. A similar effect was observed in [47] where monatomic steps on Ag(110) were moved along a distance of several 100 Å at a tunnelling resistance > 4 GΩ. The destruction is more pronounced with $\{111\}$ step substrates.

4.2. A regime

Figure 11 shows two STM topographies of the Cu(223) surface with (a) 0.34 and (b) 0.5 ML of Ag. Both correspond to the A regime, which is characterized by a fairly regular hill-and-valley structure of Ag-covered facets oriented in the (112) direction and clean Cu stepped areas. The inset of figure 11(a) shows a closer view of the surface, where one can observe a coarsely corrugated stripe, attributed to a Moiré[6] pattern in the Ag-covered facet, as well as the monatomic steps at clean Cu stripes with their typical frizzy edges. The AES cross-check allows us to ensure that Ag cannot significantly be present at the clean Cu areas in between the Ag stripes. This analysis is based on the assumption that the thickness of the Ag stripes is a single adlayer, and surface alloying can be ruled out [55]. A reference for the calibration of the Ag Auger signal was made by means of 1 ML Ag films.

In figure 12 we show the schematic profile of the Ag/Cu nanostructure. The local orientation of the Ag-covered facets in the A regime is always (112), independent of the coverage. (112) is a crystal plane that deviates by 19.5° with respect to the (111) plane. Such facet orientation is deduced from STM linescan analysis. As observable in figure 11 increasing the Ag coverage in the A regime results in a higher density of Ag-covered stripes and a reduction of the step density within the clean Cu bands. The latter is due to the fact that Cu(112) facets ($d_{112} = 6.25$ Å, $2\frac{2}{3}$ atomic rows per terrace) have higher step density than the average surface, thus their relative growth requires additional steps from Cu stripes.

At 0.34 ML the hill-to-hill distance is 140 Å and the width of the Ag and Cu stripes is 49 and 91 Å, respectively. For this reason, the local miscut at Cu stripes is $\varphi^{Cu} = 8.1°$; this is in

[6] Moiré (probably French) denotes a pattern that is caused by interference between two sets of fine pattern grids, typically referred to as distortions in the context of textile or printing techniques.

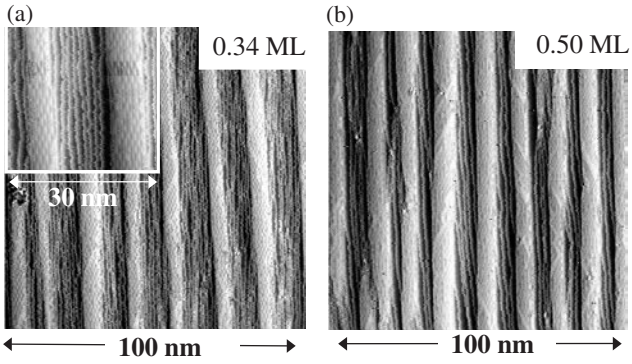

Figure 11. STM images measured at different coverages for Ag-induced faceting in vicinal Cu(111). The system displays periodic, two-phase separation of Ag-covered (112) facets and clean Cu stepped stripes. (a) An Ag coverage of 0.34 ML. The inset shows the Moiré reconstruction of the (112) Ag facet in detail. As the Ag coverage increases from (a) to (b), steps from Cu stripes incorporate in Ag facets, such that Cu terraces become wider. This is proven by the splitting reduction in the LEED pattern (see figure 14 below, taken from [56]).

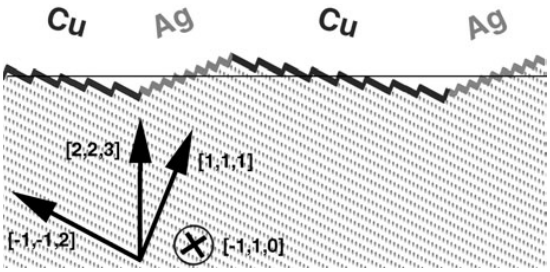

Figure 12. Lateral profile of the Cu/Ag superlattice. The global (initially also local) miscut of the surface is $\varphi_{\mathrm{Cu,initial}} = 11.4°$, which corresponds to the (223) plane. The angle of the Ag facet with respect to (111) is always $\varphi_{\mathrm{Ag}} = 19.5°$, i.e. (112). Here the case of figure 11(a) with 0.34 ML of Ag is shown. Then the angle of the clean Cu stripes is $\varphi_{\mathrm{Cu,local}} = 8.1°$, which is the (334) facet (from [17]).

between the miscut of the initially clean surface and the flat (111) orientation. At 0.50 ML the hill-to-hill distance reduces to 90 Å and the width of the Ag and Cu stripes changes to ∼44 and ∼46 Å, respectively. The local miscut within the Cu stripes becomes very low at such high coverages. The average local miscut inside the Cu stripes is $\varphi^{\mathrm{Cu}} = 5°$. Flat Cu(111) facets with 0° miscut would be reached at a coverage of 0.59 ML (see equation (1) below).

Figure 13 shows the step rearrangement in detail. The vertical black bars mark the step edges. The upper part shows a 300 Å cut-out of an STM topography with 0.34 ML Ag. For direct comparison the lower part of figure 13 shows a 300 Å cut-out of a clean Cu(223) surface. The step density within the Ag stripes is higher than in the clean Cu stripes. The step density in the Cu stripes depends on a change in the Ag coverage. Clean Cu stripes and Ag-covered facets have a step density of $\rho^{\mathrm{clean}} = \rho^{223} = (10.2\ \text{Å})^{-1}$ and $\rho^{\mathrm{Ag}} = \rho^{112} = (6.25\ \text{Å})^{-1}$, respectively. The following equation gives directly the local miscut of the clean Cu stripes:

$$\rho^{\mathrm{Cu}}(\Theta) = \frac{1}{1-\Theta}\rho^{\mathrm{clean}} - \frac{\Theta}{1-\Theta}\rho^{\mathrm{Ag}} = \rho^{\mathrm{clean}} + \frac{\Theta}{1-\Theta}(\rho^{\mathrm{clean}} - \rho^{\mathrm{Ag}}). \quad (1)$$

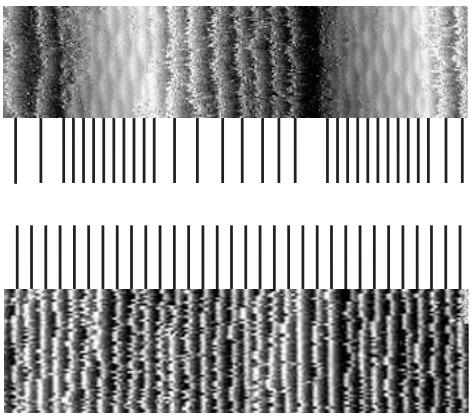

Figure 13. Step density on Ag-covered Cu(223)(top) and clean Cu(223)(below). The black bars mark the step edges. The Ag coverage reduces the step density in the clean Cu stripes which results in a change of the local orientation of the local Cu facet.

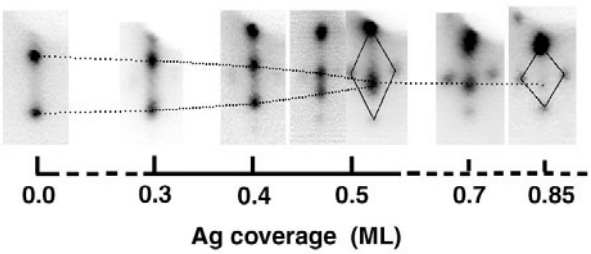

Figure 14. (0, 0) LEED spot measured at different coverages for Ag-induced faceting in vicinal Cu(111). Up to 0.6 ML, the system displays periodic, two-phase separation of Ag-covered (112) facets and clean Cu stepped stripes. Both give distinct LEED structures, i.e. spot splitting for Cu stripes (marked by the dotted lines) and Moiré pattern spots for Ag facets (indicated by rhombuses). As the Ag coverage increases, steps from Cu stripes incorporate in Ag facets, such that Cu terraces become wider. This is proven by the reduction of the splitting (from [56]).

Note that this nanostructure allows a continuous control of the local miscut of the Cu stripes via Ag coverage at this range of coverage. This is of interest because the continuous change of the local miscut at clean Cu stripes is reflected in the electronic structure [57, and article by Mugarza and Ortega in this issue]. Typically, the binding energy and orientation of the reference plane of the the Shockley surface state change with miscut [58].

The change of the local miscut and the effective step removal from Cu stripes is also followed in the LEED pattern in figure 14. In the LEED pattern we have both the spot structure from the Ag Moiré and the splitting from the step array in the Cu stripe. The Cu splitting smoothly shrinks as a function of Ag coverage, and both spots merge into a single one with 0.52 ML, when the A regime saturates[7].

SPA-LEED measurements were made at coverages within the A regime at 0.45 ML, $\varphi_{\mathrm{Cu,local}} = 6°$ [25]. This time the linear $k_{\parallel}$-scans were taken along the $[-3, -3, 4]$ direction of the hill and valley Ag–Cu structure (figure 15). They are plotted in a grey scale representation as a vertical cut of reciprocal space with the parallel and vertical k-vector as x- and y-axes.

[7] The A regime ideally saturates at 0.61 ML, when Cu stripes become flat (111) terraces [17]. However, some steps appear pinned by defects within Cu stripes, such that the effective saturation coverage is lower.

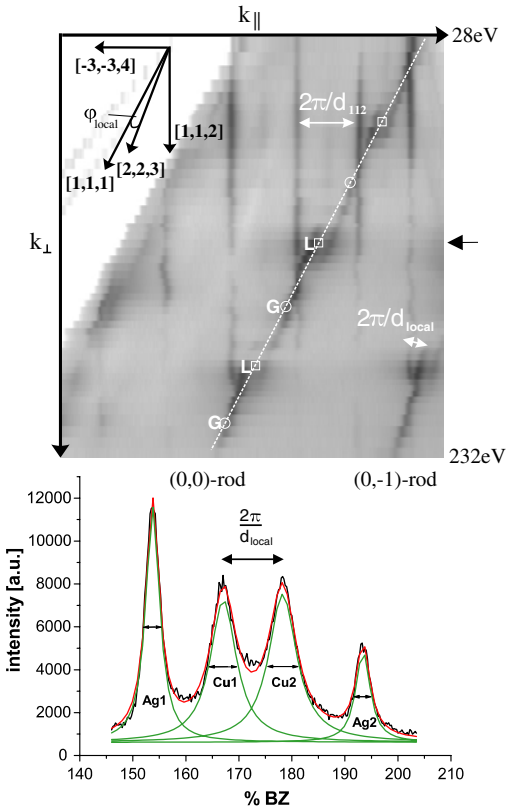

Figure 15. Vertical cut of reciprocal space along the $[-3, -3, 4]$ direction of the hill and valley Ag–Cu structure. Intensity is shown as a logarithmic grey scale plot. Vertical black lines represent the $(0, 1)$ and $(0, 0)$ rods. The linear $k_{\parallel}$-scans were horizontally shifted to scale the vertical $k_{\perp}$-direction along the [1,1,2] direction of the Ag covered facets. Thus the *vertical* black lines derive from the Ag-covered (112) facets and the *tilted* black lines derive from the clean Cu stripes. The separation of the Cu rods is $2\pi/d_{\mathrm{local}}$. The lower part shows the anti-phase condition at 100 eV in detail (marked with a black arrow). The experimental data were fitted with a Lorentzian curve. From the FWHM domain widths D can be deduced.

Furthermore, the linear $k_{\parallel}$-scans were horizontally shifted to scale the vertical $k_{\perp}$-direction along the [1,1,2] direction of the Ag covered facets. Now the structural information of both the Ag and Cu stripes can be observed in the $k_{\parallel}$-scans. Thus the *vertical* black lines derive from the Ag-covered (112) facets and the *tilted* black lines derive from the clean Cu stripes. The separation of the Cu rods corresponds to $2\pi/d_{\mathrm{local}}$ (see figure 15). Note that the intensity modification with increasing $k_{\perp}$ is negligible. This demonstrates the missing periodicity perpendicular to the Ag-covered facet, indicating a Ag film-width of only 1 ML. The black arrow marks the anti-phase condition at 100 eV (L-point). The lower part of figure 15 shows the the spot profile in detail. The x-axis is scaled in % Brillouin zone. A first qualitative analysis of the $k_{\parallel}$-scans gives $d_{\mathrm{Cu,local}} = 21$ Å at a Ag coverage of 0.45 ML. This value is compatible with the STM data. The Ag peaks are separated by $2\pi/d_{112}$. It is particularly interesting to perform a quantitative spot profile analysis to determine the characteristic domain width for the Ag/Cu stripes, because their width lies below the transfer width of SPA-LEED. Therefore, we have to analyse the linear $k_{\parallel}$-scans along the $[-3, -3, 4]$ direction.

The experimental data were fitted by a Lorentzian curve and the FWHM obtained was averaged over all Cu and Ag peaks in the linear $k_{\parallel}$-scans. The domain with D is given

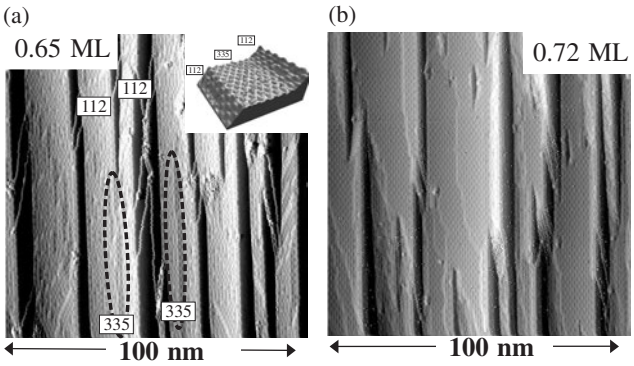

Figure 16. STM images measured at a coverage of 0.65 ML (a) and 0.72 ML (b) Ag. The system still displays periodic, two-phase separation of Ag-covered (112) facets and clean Cu stepped stripes. The dashed areas in figure (a) show the development of (335) areas directly from the centre of pre-existing (112) facets. The inset shows a 3D representation of the dashed areas. The different periodicity of the (335) Moiré is directly proven by change in the dimensions of the rhombuses according to figure 14.

approximately by $D = 2\pi/\mathrm{FWHM}$. For a coverage of 0.45 ML Ag we obtain a domain width for the Ag and Cu stripes $D_{\mathrm{Cu}} = 42 \pm 5$ Å and $D_{\mathrm{Ag}} = 73 \pm 5$ Å. The domain width of the Cu stripes D_{Cu} of 42 ± 5 Å is compatible with the Cu stripe width measured with STM (45 Å). The domain width of the Ag stripes (D_{Ag} of 73 ± 5) does not match with the $\approx$40 Å measured with STM. It is surprising that the Ag diffraction beams are narrower than expected, because it is generally easier to discuss causes for peak broadening, like dynamics or disorder, but relatively difficult to reason about narrowed diffraction peaks. From the STM images two clues can be gained that may support the Ag diffraction peaks being narrower than the Cu peaks: first, the Ag Moiré pattern is better ordered than the step array within the Cu stripes. Another factor is the very good definition of the orientation of the Ag facet orientation compared to the less defined orientation of the Cu antistripes. Furthermore, it is surprising that no appreciable shoulders or deviation from the Lorentzian shape in the peaks is found. Weak shoulders in the spot profile would be plausible with uniform stripe width and spacing [59]. However, weak shoulders can also easily be obscured by other effects affecting the coherence.

In summary, SPA-LEED measurements of Ag-covered Cu(223) give additional information on the domain size parameters; the obtained coherence lengths are only in qualitative agreement with the domain sizes resulting from the STM measurements.

4.3. B regime

Beyond 0.52 ML the A regime cannot be continued, because there are no steps left in the Cu antistripes that could be used to extend the Ag stripe facet. The B regime from 0.52 to 0.76 ML is characterized by a smooth transition in the Ag-covered facet orientation from (112) to (335). Figure 16 shows two STM images within the B regime. (335) is a crystal plane that deviates by 14.4° with respect to the (111) plane. Such facet orientation is deduced from STM linescan analysis. The latter is closer to the surface normal, allowing a higher Ag saturation. (335)-covered areas develop directly from the centre of pre-existing (112) facets or arise by melting two contiguous (112) facets (dashed areas in figure 16(a)). In both cases, the (335) orientation characterizes the centre of the Ag-covered stripes, whereas the boundaries preserve the (112) orientation. The inset of figure 16(a) shows a 3D representation of an area where

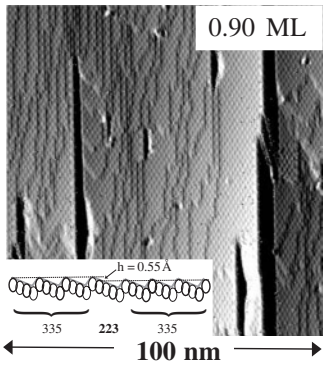

Figure 17. STM topography of the Cu(223) surface covered with 0.9 ML Ag: large areas with Ag-covered (335) facets and few uncovered (111) terraces (black patches) can be seen. The weak vertical lines within the Ag layer originate from single (223) steps between the (335) facets. As shown in the inset a (223) step yields an additional height difference of $h = 0.55$ Å.

the (335) facet lies between two (112) facets. It is easy to see the difference in their deviation with respect to the (111) plane. At 0.65 ML the hill-to-hill distance is 100 Å and the width of the Ag and Cu stripes is 60 and 40 Å, respectively. For 0.72 ML (shown in figure 16(b)) the B regime is almost saturated, i.e. we have flat Cu(111) terraces and mostly (335)-oriented Ag stripes, also displaying a Moiré structure (but different Moiré than within the A regime). The step separation for the (335) facet is $d_{335} = 8.4$ Å ($3\frac{2}{3}$ atomic rows per terrace). At 0.72 ML the hill-to-hill distance is 110 Å and the width of the Ag and Cu stripes is 90 and 40 Å, respectively.

4.4. C regime

Beyond 0.76 ML the B-regime evolution is replaced by another type of structural development. In the C regime, between 0.76 and 1 ML, (223) facets develop. Figure 17 shows an STM image of the C regime (0.9 ML Ag). The image shows a nearly close-packed Ag layer covering a random distribution of (335) and (223) terraces. The (223)-like terraces have the same step density as the initial substrate surface and can be identified by means of the additional small steps (weak vertical lines). These additional steps seem to descend from left to right, thus in the opposite direction to the substrate steps. The inset of figure 17 shows a schematic structural model of the additional small steps. The step separation for the (223) facet is $d_{223} = 10.5$ Å ($4\frac{2}{3}$ atomic rows per terrace). Therefore (223) facets in between two (335) facets ($3\frac{2}{3}$ atomic rows per terrace) result in a height difference of 0.55 Å, as observed in the STM topographies. With 1 ML we observe a close-packed Ag layer wetting a random distribution of (335)- and (223)-like terraces.

4.5. Microscopic driving force

On the atomic scale, the driving force for the Ag-induced faceting of the stepped Cu surface is a compromise in matching between Ag(111)-like packed rows along the parallel direction of the steps and the Cu facet underneath. The Ag(111) layer quasi-retains its Ag-like lattice spacing which exceeds by 13% that of Cu. On the other hand the rotational degree of freedom is used to reach some commensurability. Lattice matching, which lowers the strain contribution to the stress energy [4, 5], has been also proposed as the microscopic mechanism for the NaCl-induced

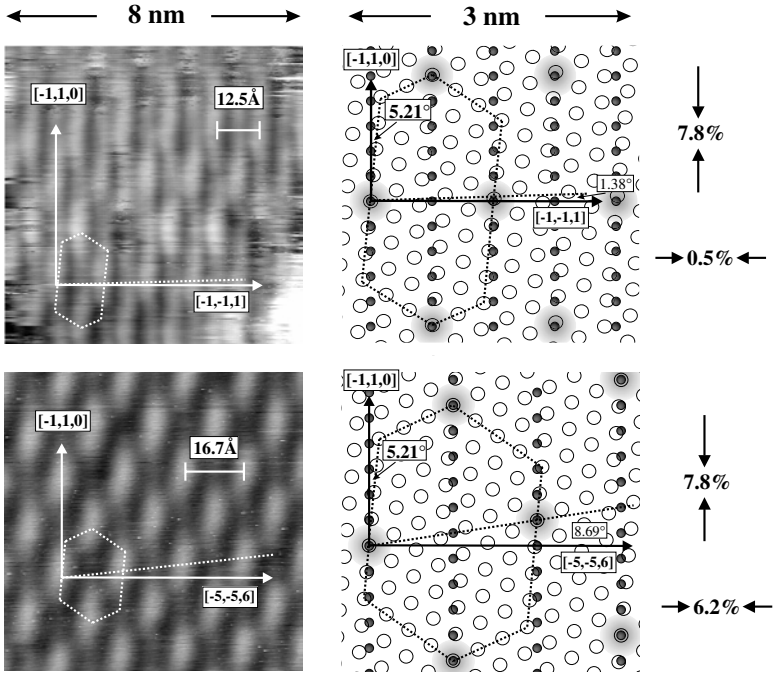

Figure 18. Left, detailed STM view of the Moiré patterns for (112) and (335) Ag-covered facets. The mean corrugation amplitudes of the Moiré structures are 0.6 Å. Right, two-dimensional atomic models that reproduce the Moirés on the left. The small filled circles indicate the step edge Cu atom positions underneath. Open dots represent Ag atoms and shaded circles indicate 'on-top' positions. The fit requires the indicated compressions and azimuthal rotations of the Ag packed layer (from [56]).

faceting of Cu(112) [18]. Our system generally displays a clear tendency to avoid adsorption on wide (111) terraces, which leads to a large mismatch [60]. On the other hand, as the analysis revealed (figures 11 and12), there is a preference for (112)-oriented facets at low coverages, although that this requires a larger mass transport. This can be straightforwardly explained by the width of the Cu terrace required for a good matching in the perpendicular direction. Five Ag packed rows (2.498 Å wide each) fit two 6.25 Å wide terraces in Cu(112) with only 0.12% mismatch in the direction perpendicular to the steps, whereas Cu(335) requires two 8.37 Å wide terraces to accommodate seven Ag rows with 4.47% mismatch. This preference for (112) facets is also supported by the microscopic analysis of (112) and (335) stripes shown in figure 18. The atomic models in the right-hand panels of this figure reproduce the Moiré patterns of the left-hand panels in the simplest way. The open circles represent Ag close-packed layers, the small dots the Cu(112) and Cu(335) unit cell underneath, and the shaded circles the 'on-top' positions.

We use the smallest compressions and azimuthal rotations of the Ag(111) adlayer to obtain the Moirés that fit the STM observations. For both (112)- and (335)-oriented layers the Ag layer rotation is the same, 5.2°, allowing the smooth transition from (112) to (335) facets observed beyond 0.52 ML. For (112) facets the Ag adlayer is compressed by 0.5% and 7.8% in the direction perpendicular and parallel to the rows, respectively. For (335) facets the perpendicular and parallel compressions are 6.2% and 7.8%, respectively. Thus, the (335)-oriented layer accumulates much more strain, explaining the preference to form (112)-oriented stripes.

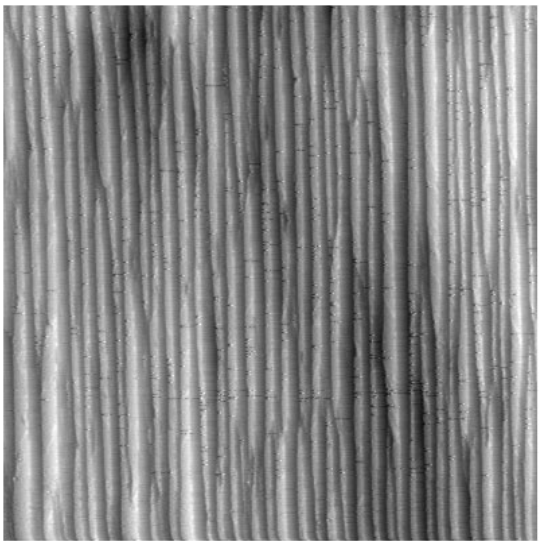

Figure 19. STM topographies of the same Cu(223) surface as in figure 11(b), taken at a region with 0.50 ML Ag. The large scale (3250 Å × 3250 Å) image shows the limited coherence of the lateral superlattice. The mean corrugation amplitudes of the hill-and-valley structures are 7 Å (taken from [17]).

Larger (223) patches have not been observed inside the C regime. Nevertheless, a model for the Ag Moiré pattern can be discussed that matches with the (223) orientation of the substrate steps inside the Ag stripes (not shown). Again, a 5.2° azimuthal rotation of the Ag(111) layer has to be chosen to ensure the continuous transition from (335) to (223) facets. The compression parallel to the substrate steps remain 7.8% but the perpendicular compression is slightly increased to 6.5%. Therefore this Ag Moiré on a (223) facet represents the energetically most unfavourable situation among the three.

In summary, the system chooses the orientation of the Ag covered facets in the same order as the perpendicular strain increases for the Ag Moiré.

Note that the growth of the Ag layer is a very special case. The adsorbed film keeps its own lattice constant but still reaches matching or commensurability with a certain substrate facet by an azimuthal rotation of the Ag(111) layer. The growth of a rotated Ag(111) layer was suggested first in an STM study for Ag/Cu(111) [61].

4.6. Long range order

An important question is what determines the mesoscopic period of the hill-and-valley structure. Figure 19 shows the limited lateral coherence of the Ag/Cu mesoscopic structure at a coverage of 0.5 ML. The decay length of the autocorrelation function is three to five periods in the direction perpendicular to the stripes (stronger autocorrelation with coverages close to 0.5 ML), whereas the Ag stripes inside regular patches are longer than 3000 Å. Statistical evaluations of images of (2000 Å)^2 size yield distributions of Gaussian type with standard deviations of $0.25\langle width\rangle$ for the hill-to-hill-distance, the Ag stripe-width and the Cu stripe-width. This is the best superlattice we can obtain under these preparation conditions. The coverage range between 0.3 and 0.5 ML is the optimum to obtain Ag/Cu superlattices. At coverages below 0.3 ML the length of the Ag-covered stripes is very much reduced. Above

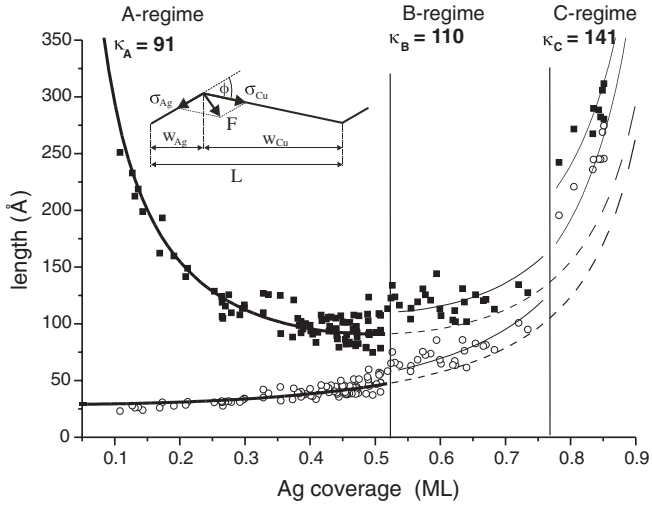

Figure 20. Nanostructure periodicity (filled squares) and Ag-covered stripe width (open circles) as a function of Ag coverage (from [56]). Vertical lines distinguish the A, B and C regimes, which differ in the type of growing Ag-covered facet. The thick solid lines are fitted to the data in the two-phase A regime using the continuum elastic theory of Marchenko [62]. A continuation in the B–C regimes is represented by the thin dotted line. The thin solid lines do fit separately data points in the B and C regime. The inset shows the surface stress vectors in a faceted structure (see the text).

0.52 ML (B and C regimes) there is a transition to a structure with melted Ag stripes, as mentioned above.

4.6.1. Variation of the period. In the following we analyse the long range period of the Ag-induced faceting as observed in STM topographies (figures 11,16 and17). Data points in figure 20 represent the nanostructure period (L) and the Ag stripe width (w_{Ag}) measured from the STM images as a function of coverage (θ) from 0.1 to 0.9 ML. The periodicity is poorly defined above 0.52 ML, and in this case we consider the average value $\langle L\rangle$, defined as $\langle L\rangle = \langle w_{\mathrm{Ag}}\rangle + \langle w_{\mathrm{Cu}}\rangle$, where $\langle w_{\mathrm{Ag}}\rangle$ and $\langle w_{\mathrm{Cu}}\rangle$ respectively are the average widths of Ag-covered facets and Cu stripes. Data points at regime transitions display a clear discontinuity. Microscopically, this appears related to the way the new facets develop, i.e. by melting two contiguous Ag stripes in the previous regime.

4.6.2. Application of elastic theory. Both Cu and Ag stripe widths can be varied smoothly in the 3–30 nm range by tuning Ag coverage. This makes the Ag/Cu(223) system particularly interesting for a quantitative test of theoretical faceting models. The surface structure will take a compromise solution between an infinite period (no domain boundaries but extensive strain) and a short periods (many domain boundaries but effective relaxation). In the simplest approach, the coverage-dependent long range periodicity can be explained within Marchenko's elastic theory [62]. The lines in figure 20 are fitted to the data using Marchenko's model, where the superlattice periodicity L and the stripe width w_{Ag} are given by

$$L(\theta) = \frac{\kappa}{\sin(\pi\theta)}; \qquad w_{\mathrm{Ag}}(\theta) = \frac{\kappa\theta}{\sin(\pi\theta)}. \tag{2}$$

κ is the only adjustable parameter. Restricting the fit to the A regime we obtain $\kappa_A = 91 \pm 6$ Å. The fit is excellent, demonstrating that inside this regime the value for κ appears not to depend appreciably on coverage. This gives evidence that the elastic theory for continuous media is applicable here. As indicated by the dashed lines in figure 20, data points at higher coverage regimes cannot be fitted with κ_A. By changing in equation (2) to $\kappa_B = 110 \pm 8$ Å and $\kappa_C = 141 \pm 8$ Å both $\langle w_{Ag}(\theta)\rangle$ and $\langle L(\theta)\rangle$ in B and C regimes, one can still obtain a good agreement with Marchenko's model. We conclude that this simple theory is applicable in this system, but with different values of κ in each facet-type regime.

4.6.3. What can one learn from κ? In Marchenko's approach κ is related to elastic constants via

$$\kappa = 2\pi a \exp(1 + C_1/C_2), \tag{3}$$

where a is a characteristic microscopic cut-off of the order of atomic distances and C_1 is the free energy of the phase boundary per unit length [62]. If we assume that work function variations between Cu and Ag phases are relatively small [63], C_2 has only elastic nature and reflects the stress difference between phases [62]: $C_2 = \frac{1-\nu 2}{\pi E}|\vec{F}|^2$ where E and ν respectively are the shear modulus and the Poisson ratio for Cu. In this formula $|\vec{F}|^2 = (\vec{\sigma}_{Ag} - \vec{\sigma}_{Cu})^2 = \sigma_{Ag}^2 - 2\sigma_{Ag}\sigma_{Cu}\cos\phi + \sigma_{Cu}^2$ is the force exerted at facet edges due to the difference in surface stress $\vec{\sigma}$ between Ag-covered facets and Cu stripes and ϕ stands for the angle between adjacent facets, as shown in the inset of figure 20. Therefore, κ is related to three independent, unknown constants a, C_1 and C_2, which in turn cannot be determined from the experiment. Literature values are not available with sufficient accuracy for such complex systems.

Nevertheless, it is interesting to discuss the potential influence of the three parameters a, C_1 and C_2 on the characteristic lengths assuming the elastic model of equations (2) and (3). First we note that the good fit of equation (2) to data points in the A regime discards any remarkable coverage dependence in κ. Such coverage dependence is indeed expected for C_2 via changes in σ_{Cu} (changes in $\cos\phi$ are too small). In Au(111) vicinals [64], the intrinsically stressed (111) plane is relaxed in the presence of steps, such that σ decreases as a function of $\tan\varphi$, where φ is the local miscut with respect to the (111) surface. Assuming the same behaviour for Cu(111), we expect an increase of σ_{Cu} of about 20% as a function of Ag coverage in the A regime. In contrast, the structure of the Ag stripes remains unchanged and hence σ_{Ag} stays constant for the A regime. Thus the absence of a coverage dependence suggests the dominant effect of σ_{Ag} ($\sigma_{Ag} \gg \sigma_{Cu}$) in C_2. According to our model in figure 18, there is indeed a high stress energy in the Ag-covered facets due to strain, particularly in the direction parallel to the steps where the Ag layer is largely compressed.

In Au(111) faceting a variety of periodicities are found as a consequence of the delicate balance between the (constant) boundary energy C_1 and the facet-type-dependent C_2 [64]. The boundary energy in that case is of the order of the step energy, which displays minor variations for all noble metal surfaces [29]. In our Ag-induced faceting, C_1 can be assumed to be the energy needed to add or remove a Ag(111) atomic row, i.e. also of the order of the Ag(111) step energy. But in our case, since C_2 appears to be determined by a high σ_{Ag}, the boundary energy will surely be unbalanced by the stress constant C_2. Therefore, despite the fact that the stress situation must be different for all three regimes, we expect $C_1/C_2 \sim 0$ in the whole coverage range due to the high stress of the Ag-covered facets.

4.6.4. The cut-off length. Note that if $C_1/C_2 \sim 0$ in figure 20, the changes in κ at different regimes must be mostly explained by changes in the cut-off length a. The physical nature of a

is not clear in elastic theory. Although it appears as an artificial way of avoiding divergence in energy integrals [62], it should be understood as the minimum size of the domains, from which one has to integrate [63]. For clean, non-reconstructed surfaces the natural choice of a is thus the atomic row distance in terraces [64]. In vicinal Si(111) the facet width is a multiple of the (7×7) unit cell, which thereby defines the cut-off length [65].

Following these arguments, in Ag/Cu faceting one can take the cut-off length as the minimum size of the (growing) Ag-covered facet, i.e. the terrace width underneath. This is indeed supported by a close evaluation of STM topographs, which clearly show Ag stripes growing laterally by multiples of the terrace width d of the underlying Cu facet, i.e. $d_{112} = 6.25$ Å, $d_{335} = 8.4$ Å and $d_{223} = 10.5$ Å in A, B and C regimes, respectively. Assuming $C_1/C_2 = 0$ in equation (3) and using the different values of κ obtained in the separate fits in figure 20, we obtain $a_{112} = 5.3$ Å, $a_{335} = 6.4$ Å and $a_{223} = 8.3$ Å. The order of magnitude and the growing trend is correct, although the absolute numbers still come 15–25% lower with respect to the terrace width.

On the other hand, assuming a constant cut-off length of the order of the atomic separations in the whole coverage, the discontinuities of figure 20 would indicate that C_1/C_2 increases from A to B and C regimes. This is unlikely, because stress relief should be more effective if the mesoscale corrugation is larger. The boundary energy C_1 must be very similar in the three regimes, because the atomic structure at facet edges, as observed in the STM figures or deduced from the Moiré analysis in figure 18, is the same. Thus the different κ-values in the separate fits would indicate that $C_2^{(112)} > C_2^{(335)} > C_2^{(223)}$, in contrast with the observation of a preferred (less stressed) (112) faceting at early coverage.

Note that the $C_1/C_2 \sim 0$ case leads to the shortest possible superlattice period in Ag/vicinal Cu(111). This contrasts with the long superlattice periods observed at high temperatures with NaCl/v-Cu(111) [18]. Long periods are only possible if $C_1/C_2 \gg 1$, which in the latter case could be due to a more efficient interface relaxation, favoured by a large adsorbate–surface charge transfer that weakens Cu–Cu bonds.

5. Summary

In summary, clean vicinal Cu(111) surfaces show regular step lattices and anisotropic dynamics with respect to the two step types along the densest-packed direction. Upon Ag adsorption an Ag–Cu stripe phase is formed. The driving forces for Ag-induced periodic faceting of vicinal Cu(111) have been studied. At the atomic scale, this phenomenon is explained by lattice matching of densely packed Ag rows with different Cu facets. On the mesoscopic scale, despite the general complexity of the system, the characteristic lengths are well explained using Marchenko's elastic theory at thermal equilibrium. We observe coverage-dependent discontinuities of the faceting periodicity related to the successive appearance of different Ag-covered facet orientations. A semi-quantitative analysis within Marchenko's model indicates a high stress energy in Ag-covered facets and a different cut-off length at different facet-type regimes.

Acknowledgments

The SPA-LEED measurements have been performed in collaboration with K Schwinge, J J Paggel and P Fumagalli, *Freie Universität Berlin*. ARB and SS are supported by the Stichting voor Fundamenteel Onderzoek der Materie (FOM) and the Deutsche Forschungsgemeinschaft (DFG). FO is supported by the DFG.

References

[1] Drexler E and Peterson C 1991 Unbounding the Future http://www.foresight.org/UTF/Unbound_BW/index.html
[2] Compano R 2000 *Technology Roadmap for Nanoelectronics* ftp://ftp.cordis.lu/pub/ist/docs/fetnidrm.zip
[3] Moriarty P 2001 Nanostructured materials *Rep. Prog. Phys.* **64** 297
[4] Shchukin V A and Bimberg D 1999 *Rev. Mod. Phys.* **71** 1125
[5] Ibach H 1997 *Surf. Sci. Rep.* **29** 195
[6] Rousset S, Repain V, Baudot G, Ellmer H, Garreau Y, Etgens V, Berroir J M, Croset B, Sotto M, Zeppenfeld P, Ferre J, Jamet J P, Chappert C and Lecoeur J 2002 *Mater Sci. Eng.* B **96** 169
[7] Reinecke N, Reiter S, Vetter S and Taglauer E 2002 *Appl. Phys.* A **75** 1
[8] Teichert C 2002 *Phys. Rep.* **365** 335
[9] Brune H, Giovannini M, Bromann K and Kern K 1998 *Nature* **394** 451
[10] Pohl K, Bartelt M C, de la Figuera J, Bartelt N C, Hrbek J and Hwang R Q 1999 *Nature* **397** 238
[11] Hannon J B, Tersoff J and Tromp R M 2002 *Science* **295** 299
[12] Nötzel R, Niu Z C, Ramsteiner M, Schonherr H P, Tranpert A, Däweritz L and Ploog K H 1998 *Nature* **392** 56
[13] Plass R, Last J A, Bartelt N C and Kellog G L 2001 *Nature* **412** 875
[14] Seehofer L *et al* 1995 *Surf. Sci.* **329** 157
Aoki K *et al* 1998 *Surf. Sci.* **408** 101
Minoda H *et al* 1999 *Surf. Sci.* **432** 69
[15] Himpsel F J *et al* 2001 *J. Phys.: Condens. Matter* **13** 1
[16] Minoda H *et al* 1999 *Phys. Rev.* B **59** 2363
Horn von Hoegen M *et al* 1999 *Surf. Sci.* **433–435** 475
[17] Bachmann A R *et al* 2001 *Phys. Rev.* B **64** 153409
[18] Fölsch S *et al* 2000 *Phys. Rev. Lett.* **84** 123
Fölsch S *et al* 2002 *Surf. Sci.* **497** 113
[19] Himpsel F J and Ortega J E 1992 *Phys. Rev.* B **46** 9719
[20] Bachmann A R 2002 Gestufte Cu-Oberflächen und Ag-Nano-Streifen: atomare und elektronische Struktur *Dissertation* Uni. Osnabrück http://elib.ub.uni-osnabrueck.de/publications/diss/E-Diss200_thesis.pdf
[21] Henzler M 1976 *Appl. Phys.* A **9** 11
[22] Henzler M 1977 *Electron Spectroscopy of Surface Analysis* (*Springer Topics in Current Physics* vol 4) ed H Ibach (Berlin: Springer) p 117
Henzler M 1982 *Appl. Surf. Sci.* **11/12** 450
[23] Henzler M 1988 *The Structure of Surfaces II* (*Springer Series in Surface Science* vol 11) ed J F vander Veen and M A van Hove (Berlin: Springer)
Henzler M, Horn-von Hoegen M and Kohler U 1992 *Festkörperprobleme* (*Advances in Solid State Physics*) (Braunschweig: Vieweg) p 333
[24] Wollschläger J, Falta J and Henzler M 1990 *Appl. Phys.* A **50** 57
[25] Bachmann A R, Ostendorf F, Speller S, Ortega J E, Schwinge K, Paggel J J and Fumagalli P 2003 at press
[26] Giesen M, Linke U and Ibach H 1997 *Surf. Sci.* **389** 264
[27] Hecquet P and Salanon B 1996 *Surf. Sci.* **366** 415
[28] Giesen M and Schulze Icking-Konert G 1999 *Surf. Rev. Lett.* **6** 27
[29] Giesen M 2001 *Prog. Surf. Sci.* **86** 1
[30] Klas T, Fink R, Krausch G, Platzer R, Voigt J, Wesche R and Schatz G 1988 *Europhys. Lett.* **7** 151
[31] Frenken J W M and Stoltze P 1999 *Phys. Rev. Lett.* **82** 3500
[32] Benndorf C and Meyer L 1990 *J. Vac. Sci. Technol.* A **8** 2677
[33] Hahn E, Schief H, Marsico V, Fricke A and Kern K 1994 *Phys. Rev. Lett.* **72** 3378
[34] Yoon M, Mochrie S G J, Zehneer D M, Watsen G M and Gibbs D 1995 *Surf. Sci.* **338** 225
[35] Shen Q, Chang J P, Navrottski G and Blakley J M 1988 *Phys. Rev. Lett.* **7** 151
[36] Pinxteren H M v, Pluis B and Frenken J W M 1994 *Phys. Rev.* B **49** 13798
[37] Bonzel H P, Breuer U and Voigtländer B 1992 *Surf. Sci.* **272** 10
[38] Repain V, Berroir J M, Croset B, Rousset S, Garreau Y, Etgens V H and Lecoeur L 2000 *Phys. Rev. Lett.* **84** 5367
[39] Williams E D 1994 *Surf. Sci.* **299/300** 502
[40] Alfonso C, Bermond J M, Heyraud J C and Metois J J 1992 *Surf. Sci.* **262** 371
[41] Giesen M 1997 *Surf. Sci.* **370** 55
[42] Barbier L, Masson L, Cousty J and Salanon B 1996 *Surf. Sci.* **345** 197
[43] Koch R, Schulz J J and Rieder K H 1999 *Europhys. Lett.* **48** 554
[44] Joós B, Einstein T L and Bartelt N C 1991 *Phys. Rev.* B **43** 8153

[45] Le Goff E, Barbier L, Masson L and Salanon B 1999 *Surf. Sci.* **432** 139
[46] Kuipers L and Frenken J W M 1993 *Phys. Rev. Lett.* **70** 3907
[47] Li J, Berndt R and Schneider W-D 1996 *Phys. Rev. Lett.* **76** 1888
[48] Giesen M and Schulze Icking-Konert G 1998 *Surf. Sci.* **412/413** 645
[49] Maca F, Kotrla M and Trushin O S 1999 *Vacuum* **54** 113
[50] Maca F, Kotrla M and Trushin O S 2000 *Surf. Sci.* **454** 579
[51] Stumpf R and Scheffler M 1996 *Phys. Rev.* B **53** 4958
[52] Giesen M and Schulze Icking-Konert G 1999 *Surf. Rev. Lett.* **6** 27
[53] Smoluchowski R 1941 *Phys. Rev.* **60** 661
[54] Durukanoğlu S, Kara A and Rahman T S 1997 *Phys. Rev.* B **55** 13894
[55] Sprunger P T, Lægsgaard E and Besenbacher F 1996 *Phys. Rev.* B **54** 8163
[56] Bachmann A R, Speller S, Mugarza A and Ortega J E 2003 *Surf. Sci. Lett.* **526** L143
[57] Bachmann A R *et al* 2003 at press
[58] Ortega J E, Speller S, Bachmann A R, Mascaraque A, Michel E G, Närmann A, Mugarza A, Rubio A and Himpsel F J 2000 *Phys. Rev. Lett.* **84** 6110
[59] Nedelmann L *et al* 1998 *Surf. Sci.* **376** 113
[60] Meunier I *et al* 1999 *Phys. Rev.* B **59** 10910
[61] McMahon W E, Hirschhorn E S and Chiang T C 1992 *Surf. Sci. Lett.* **279** L231–5
[62] Marchenko V I *et al* 1980 *Sov. Phys.—JETP* **52** 129
[63] Vanderbilt D 1992 *Surf. Sci.* **268** L300
Kwok-On Ng *et al* 1995 *Phys. Rev.* B **52** 2177
[64] Rousset S *et al* 1999 *Surf. Sci.* **422** 33
[65] Men F K *et al* 2002 *Phys. Rev. Lett.* **88** 96105